

The Interstellar Boundary Explorer High Energy (IBEX-Hi) Neutral Atom Imager

H.O. Funsten · F. Allegrini · P. Bochsler · G. Dunn · S. Ellis · D. Everett · M.J. Fagan · S.A. Fuselier · M. Granoff · M. Gruntman · A.A. Guthrie · J. Hanley · R.W. Harper · D. Heirtzler · P. Janzen · K.H. Kihara · B. King · H. Kucharek · M.P. Manzo · M. Maple · K. Mashburn · D.J. McComas · E. Moebius · J. Nolin · D. Piazza · S. Pope · D.B. Reisenfeld · B. Rodriguez · E.C. Roelof · L. Saul · S. Turco · P. Valek · S. Weidner · P. Wurz · S. Zaffke

Received: 25 November 2008 / Accepted: 26 March 2009 / Published online: 23 April 2009
© Springer Science+Business Media B.V. 2009

Abstract The IBEX-Hi Neutral Atom Imager of the Interstellar Boundary Explorer (IBEX) mission is designed to measure energetic neutral atoms (ENAs) originating from the interaction region between the heliosphere and the local interstellar medium (LISM). These ENAs are plasma ions that have been heated in the interaction region and neutralized by charge exchange with the cold neutral atoms of the LISM that freely flow through the interaction region. IBEX-Hi is a single pixel ENA imager that covers the ENA spectral range from 0.38

H.O. Funsten (✉) · M.J. Fagan · A.A. Guthrie · R.W. Harper · K.H. Kihara · M.P. Manzo
Los Alamos National Laboratory, PO Box 1663, Los Alamos, NM 87545, USA
e-mail: hfunsten@lanl.gov

F. Allegrini · G. Dunn · D. Everett · J. Hanley · M. Maple · K. Mashburn · D.J. McComas · S. Pope · B. Rodriguez · P. Valek · S. Weidner
Southwest Research Institute, 6220 Culebra Road, San Antonio, TX 78238, USA

P. Bochsler · D. Piazza · L. Saul · P. Wurz
Physikalisches Institut, University of Bern, Sidlerstrasse 5, 3012, Bern, Switzerland

S. Ellis · M. Granoff · D. Heirtzler · B. King · H. Kucharek · E. Moebius · J. Nolin · S. Turco · S. Zaffke
University of New Hampshire, 39 College Road, Morse Hall, Durham, NH 03824, USA

S.A. Fuselier
Lockheed Martin Advanced Technology Center, 3251 Hanover St., Palo Alto, CA 94304, USA

M. Gruntman
Astronautics and Space Technology Division, Viterbi School of Engineering, University of Southern California, Los Angeles, CA 90089-1192, USA

P. Janzen · D.B. Reisenfeld
Department of Physics & Astronomy, University of Montana, 32 Campus Drive, Missoula, MT 59812, USA

E.C. Roelof
Applied Physics Laboratory, 11100 Johns Hopkins Road, Laurel, MD 20723-6099, USA

to 6 keV and shares significant energy overlap and overall design philosophy with the IBEX-Lo sensor. Because of the anticipated low flux of these ENAs at 1 AU, the sensor has a large geometric factor and incorporates numerous techniques to minimize noise and backgrounds. The IBEX-Hi sensor has a field-of-view (FOV) of $6.5^\circ \times 6.5^\circ$ FWHM, and a $6.5^\circ \times 360^\circ$ swath of the sky is imaged over each spacecraft spin. IBEX-Hi utilizes an ultrathin carbon foil to ionize ENAs in order to measure their energy by subsequent electrostatic analysis. A multiple coincidence detection scheme using channel electron multiplier (CEM) detectors enables reliable detection of ENAs in the presence of substantial noise. During normal operation, the sensor steps through six energy steps every 12 spacecraft spins. Over a single IBEX orbit of about 8 days, a single $6.5^\circ \times 360^\circ$ swath of the sky is viewed, and re-pointing of the spin axis toward the Sun near perigee of each IBEX orbit moves the ecliptic longitude by about 8° every orbit such that a full sky map is acquired every six months. These global maps, covering the spectral range of IBEX-Hi and coupled to the IBEX-Lo maps at lower and overlapping energies, will answer fundamental questions about the structure and dynamics of the interaction region between the heliosphere and the LISM.

Keywords Interstellar boundary · Termination shock · Heliopause · Energetic neutral atom · ENA · LISM

PACS 96.50.-e · 96.50.Ek · 96.50.Xy · 96.50.Zc

1 Introduction

The scientific objective of the Interstellar Boundary Explorer (IBEX) mission, launched on Oct. 19, 2008, is to discover the global interaction between the heliosphere and the local interstellar medium (LISM) (McComas et al. 2006, 2009b, this issue). By acquiring global maps of the spectral distribution of energetic neutral atom (ENA) fluxes emitted from this interaction region, IBEX will answer four fundamental questions:

- I: What is the global strength and structure of the termination shock?
- II: How are energetic protons accelerated at the termination shock?
- III: What are the global properties of the solar wind flow beyond the termination shock and in the heliotail?
- IV: How does the interstellar flow interact with the heliosphere beyond the heliopause?

Hydrogen ENAs are generated when solar wind or pickup protons, which are heated at or near the shocked interface between the solar wind and the local LISM, are neutralized by charge exchange with the cold neutral atoms that constitute a majority of the LISM (Gloeckler and Geiss 2004) and freely flow through the interaction region. A fraction of these ENAs successfully travel from the point of their neutralization to 1 AU, avoiding photoionization from solar UV and ionization by either impact with solar wind electrons or charge exchange with solar wind ions. Because the ENAs detected by IBEX-Hi have followed ballistic trajectories from their emission region beyond the edge of the termination shock, their flux and spectral distribution provide key signatures of the global nature of the structure and dynamics of the interaction between the heliosphere and the LISM.

The IBEX science payload consists of two ENA imaging sensors that act as highly sensitive single pixel cameras. They utilize the Common Electronics Unit (CEU) for sensor control, conditioned power, data processing, and telemetry management. While similar in functional design, these sensors are optimized to measure the tenuous ENA flux across two

overlapping energy ranges: the IBEX-Lo sensor (Fuselier et al. 2009, this issue) measures ENAs from ~ 10 eV to 2 keV in eight energy steps, and the IBEX-Hi sensor measures ENAs from ~ 380 eV to 6 keV in six energy steps. The difference in energy ranges covered by the sensors is enabled by the different mechanisms by which they ionize ENAs before the ionized ENAs are electrostatically energy-analyzed and detected. In the higher energy range covered by the IBEX-Hi sensor, ENA ionization (specifically $H^0 \rightarrow H^+$) by transmission through an ultrathin charge-stripping foil provides higher ionization probability, whereas in the low energy range covered by IBEX-Lo higher ionization probability (specifically $H^0 \rightarrow H^-$ and $O^0 \rightarrow O^-$) is enabled by atomic reflection from a diamond-like carbon surface. A second difference is IBEX-Lo's ability to measure ENA mass and utilize a high angular resolution collimator section to measure oxygen and uniquely address Question IV.

The ENA flux originating from beyond the termination shock and measured at 1 AU by IBEX is anticipated to lie within the range of 1 to $500 \text{ cm}^{-2} \text{ s}^{-1} \text{ sr}^{-1} \text{ keV}^{-1}$ at ~ 1 keV (Gruntman et al. 2001; Wurz et al. 2008). Because of this low ENA flux, the designs of the IBEX sensors have been driven toward maximizing the sensitivity and minimizing the noise and the backgrounds that would otherwise masquerade as ENAs. The numerous sources of background and noise (see Wurz et al. 2009, this issue) include ENAs of magnetospheric origin, ionization and acceleration of ambient gas molecules within the sensor, detection of ambient ions that are beyond the maximum rejection energy of the entrance subsystem, and coincidence events generated by penetrating radiation.

A second unique aspect of measuring these ENAs is their energy-dependent transit time from their formation beyond the termination shock to their detection by IBEX at 1 AU. This is illustrated in Fig. 1, which shows the time for a hydrogen ENA to travel 100 AU as a function of its energy. The transit times for ENAs within the energy range of IBEX-Hi to travel 100 AU range from 196 days at the central energy (4.09 keV) of the highest energy passband to 591 days at the central energy (0.45 keV) of the lowest energy passband. Furthermore, the range of travel times of ENAs emitted from a point source at 100 AU from the Earth that are detected within the full width at half maximum (FWHM) of a single energy passband ranges from 62 days at the highest energy passband to 143 days at the second lowest energy passband. This time uncertainty for an individual energy passband corresponds to $\sim 1/3$ and $\sim 2/3$, respectively, of the 6-month period over which IBEX generates a complete sky map. These time resolutions represent a lower limit because the ENA source region may be quite thick and extend significantly beyond the termination shock and because ENAs from source regions at the flanks and tail of the interaction region travel distances that can be substantially farther than 100 AU.

ENA imaging of the Earth's space environment was demonstrated serendipitously using energetic particle instruments on the ISEE-1 mission (Roelof et al. 1985) and then the Polar mission (Henderson et al. 1997). Neither these instruments nor subsequent dedicated ENA imagers (e.g., Gruntman 1997; Pollock et al. 2000; Mitchell et al. 2000; Moore et al. 2000) were optimized for the large aperture area, low noise and background, energy range, or energy resolution required to measure the dim ENA emission from the inner heliosheath.

IBEX-Hi is a high sensitivity, single pixel sensor. A critical priority of the IBEX-Hi sensor design and development was maximizing the sensitivity to ENAs while minimizing noise and backgrounds. This drove the detailed designs of each subsystem: the collimator is biased at +10 kV to reject ions up to $10 \text{ keV}/q$ and is fabricated using nonlinearly stacked thin plates having collinear aperture holes to minimize ion scattering; the charge conversion subsystem ionizes ENAs so they can be electrostatically removed from the UV and electron background; the energy analysis subsystem projects the enormous entrance aperture area of the sensor onto a small detector area and is serrated to prevent UV and ions $> 10 \text{ keV}/q$ from

Fig. 1 The *points* show the travel time for a hydrogen ENA to transit 100 AU at the central energy of each of the six IBEX-Hi energy passbands. The *error bars* at these *points* represent the travel time uncertainty due to the energy FWHM of each of the energy passbands for events detected through triple coincidence

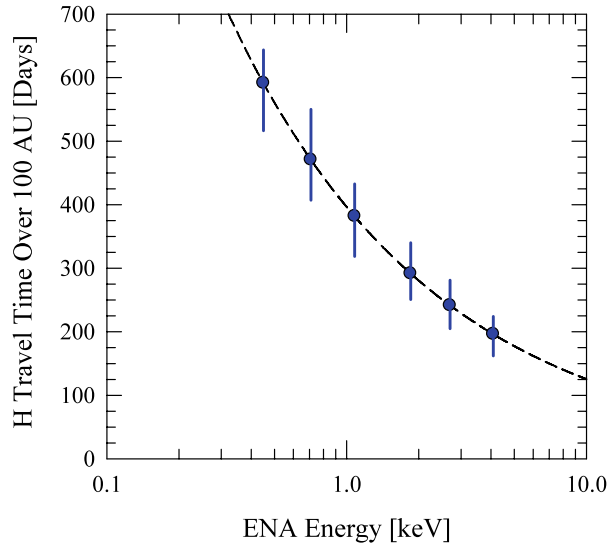


Table 1 IBEX-Hi sensor parameters and resources

Energy range	0.38–6.0 keV
Energy resolution ($\Delta E_{\text{FWHM}}/E$)	0.47–0.70
Number of energy steps	6
Field-of-view	6.5° FWHM (0.0147 sr)
Mass	7.37 kg
Power (W)	0.65 W
Telemetry	99 bps

reflecting into the detector subsystem; and the detector subsystem uses channel electron multiplier (CEM) detectors to minimize noise from penetrating radiation and to measure coincidence between these detectors to discriminate between noise and a true ENA that is detected in multiple CEMs as it transits the subsystem.

The summary of IBEX-Hi performance and resources is listed in Table 1. The next section describes in more detail the IBEX-Hi sensor subsystems and their unique designs that maximize sensitivity and minimize noise and background sufficient to view the faint ENA signal.

2 The IBEX-Hi Sensor

Figure 2 shows a cross-sectional illustration of the IBEX-Hi sensor. The sensor is divided into four subsystems that are sequentially encountered by an ENA. The entrance subsystem serves multiple purposes, including limiting the angular field-of-view (FOV) to 6.5° FWHM and electrostatic rejection of ambient electrons with energies up to 0.6 keV and ions with energies up to 10 keV/ q . The ENA then encounters the charge conversion subsystem that utilizes ultrathin carbon foils to positively ionize a fraction of ENAs that transit a foil. The ionized ENAs then enter the electrostatic energy analysis subsystem, which consists of

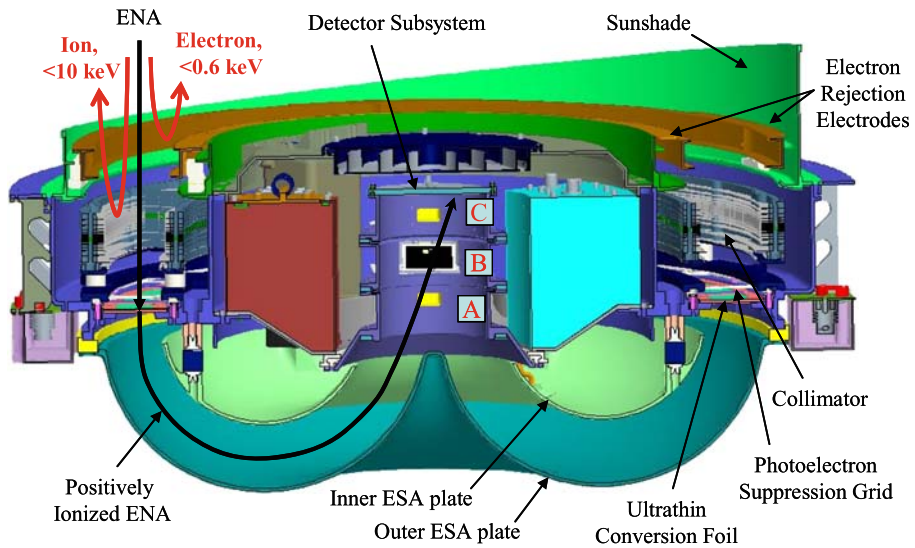


Fig. 2 This cross-sectional view of the IBEX-Hi sensor illustrates the subsystems and the trajectory of an ENA through the sensor

nested toroidal analyzer plates that project the large entrance aperture onto a small detector subsystem. The bias of the inner ESA plate sets the energy passband for ionized ENAs to enter the detector subsystem. ENAs entering the detector subsystem are accelerated by a bias of -6 kV for increased detection efficiency. The detector subsystem consists of three stacked cylindrical chambers (designated A, B, and C as shown in Fig. 2) with each chamber separated by an ultrathin carbon foil. Each chamber has a CEM detector that detects secondary electrons generated by the interaction of the ENA with a foil or an interior wall of a chamber. An ionized ENA can transit all three chambers and register a pulse in multiple detectors, generating a double (AB, BC, AC) or triple (ABC) coincidence event. The following sections describe in detail these subsystems.

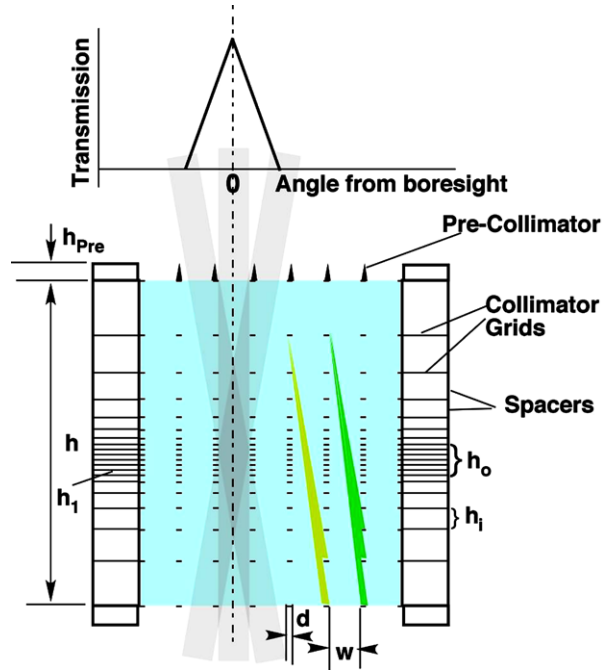
2.1 Entrance Subsystem

The IBEX-Hi collimator subsystem, which is nearly identical to that of IBEX-Lo, serves multiple purposes. First, it defines the instantaneous FOV of 6.5° FWHM. Second, appropriately biased electrodes successively prevent electrons and ions from entering the sensor aperture. Third, it limits the access of light into the sensor. The collimator has been optimized to provide maximum ENA transmission for the size and geometry of the sensor. The collimators for IBEX-Hi and -Lo are identical in their design except for small differences in inner and outer radii and a high angular resolution quadrant in IBEX-Lo that is not present in IBEX-Hi.

The collimator consists of stacked plates, each with arrays of collinear hexagonal, photoetched apertures. The use of plates minimizes the exposed surface area from which particles can scatter into the charge conversion subsystem. IBEX-Hi has the same FOV over its entire aperture.

Figure 3 shows a 2-dimensional cut through the collimator. An intrinsic complication using multiple plates with collinear apertures that form channels is leakage, in which particles with trajectories beyond the desired FOV enter one channel and can pass through to

Fig. 3 The cross-sectional cut through the collimator illustrates the sequence of identical collimator plates that successively clip trajectories of particles (e.g., ENAs, ions > 10 keV, electrons > 0.6 keV, and UV light) incident at higher angles. For example, the *yellow* and *green trajectories* represent rejection of particles that are outside of the collimator FOV. The pre-collimator prevents particles from entering at very high angles



a neighboring channel. To prevent such leakage, a series of six plates with the same small separation ($h_1 = d \tan \theta_{Max}$, where θ_{Max} is the largest possible angle of incidence of particles that must be rejected) is placed at the center of the collimator. From this set of plates in the center, additional plates are alternately stacked toward the entrance and exit ends of the collimator with the plate spacing increasing in a geometrical sequence according to $h_{i+1} = h_i(w + d)/w$ and the largest spacing at the exit plate. In the final collimator design, plate separations are slightly less than the theoretical geometric progression to account for potential leakage from manufacturing tolerances and deviations from plate planarity. The angle θ_{Max} is limited to $\leq 50^\circ$ at the collimator entrance by a precision-milled pre-collimator with trapezoid-shaped hexagon ribs, whose width is not larger than $d - 50 \mu\text{m}$.

Assuming no leakage, the angular response of the collimator is solely determined by the width w of the hexagonal openings and the total distance h between the entry and exit plates, and the FWHM is approximately $\theta_{FWHM} = \tan^{-1}(w/h)$. For a geometry with close-packed hexagonal openings in each plate, the transparency T of the collimator at normal incidence is $T = 1/(1 + d/w)^2$, where d is the width of the plate between adjacent apertures.

2.1.1 Collimator Field-of-View (FOV)

Figure 4 shows the hexagonal point spread function $P(\theta, \phi)$ of IBEX-Hi as derived using a Monte-Carlo simulation of a single hexagonal channel. The maximum transmission of 0.67 lies at $P(0, 0)$, and the integrated FOV is 0.0147 sr. Modeling of the collimator based on worst-case manufacturing and plate alignment tolerances of $100 \mu\text{m}$ indicates a cumulative transmission of $< 10^{-6}$ for particle trajectories over all angles beyond the nominal FOV. Testing of the IBEX-Lo and IBEX-Hi collimators with an Ar^+ beam showed that the combined effects of leakage through neighboring channels and scattering from edges of the collimator plates resulted in a transmission of $< 10^{-5}$.

Fig. 4 The IBEX-Hi collimator transmission as a function of incident ENA angle is derived using Monte-Carlo simulations of the geometric response of a single hexagonal channel with an aspect ratio of length h to major hexagonal cell width w of 26.83 : 1. This collimator point spread function $P(\theta, \phi)$ has a maximum transmission of 0.67 and an integrated FOV of 0.0147 sr

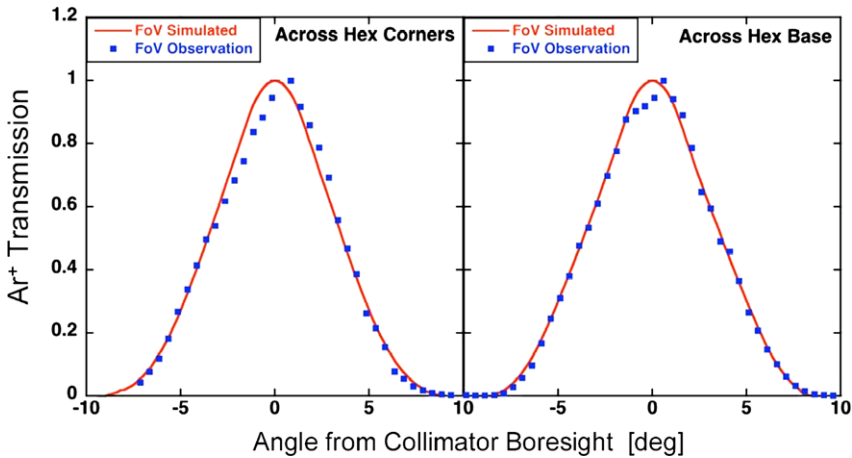
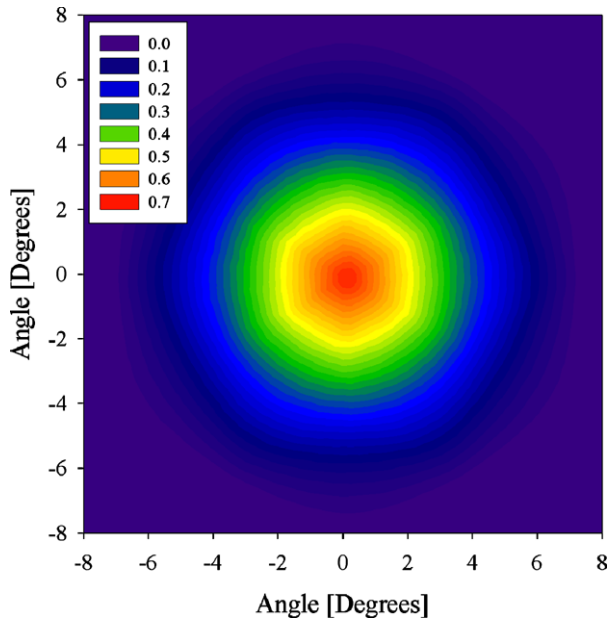


Fig. 5 Measured 20 keV Ar^+ transmission through the collimator as a function of incident beam angle θ , where $\theta = 0^\circ$ corresponds to the boresight direction, for angular scans across the hexagon corners (*left*) and across the hexagon base (*right*). The collimator was grounded during the tests. The simulated angular response is shown in *red* and agrees well with the data except near 0° , which is an artifact of non-uniform illumination of the ion beam over a small region of the collimator

The FOV and the overall transparency of the collimator were determined using an optical comparator, which measured the total line width of the collimator stack. The FOV was measured to be $6.44 \pm 0.15^\circ$ FWHM across the hexagon base and $6.5 \pm 0.15^\circ$ FWHM across the hexagon corners. The transparency of the IBEX-Hi collimator was found to be $66.85 \pm 0.75\%$. Angular and linear scans with a narrow 20 keV Ar^+ beam across the base and the corners of the hexagon have verified these optical measurements as shown in Fig. 5.

2.1.2 Suppression of Ambient Charged Particles

In order to minimize background, the IBEX sensors must reject ambient (positive) ions up to 10 keV/ q and electrons, including ubiquitous photoelectrons, up to 0.6 keV. If ions were allowed to enter IBEX-Hi, they would be indistinguishable from ENAs of similar energy. Rejection of ions up to 10 keV/ q was chosen because ion fluxes at energies >10 keV decrease rapidly with increasing energy for most plasma environments encountered over the IBEX orbit. This ion rejection is achieved by biasing the entire collimator structure to +10 kV. Furthermore, the pre-collimator imposes electrostatic troughs at the entrance of each hexagonal channel that act as defocusing lenses, so most incident ions between 10 and 16 keV are deflected to angles significantly outside the collimator acceptance range and thus are substantially prevented from reaching the conversion foil.

Figure 6 shows the observed ion transmission through the IBEX-Hi collimator as a function of incident angle for 7.5 keV Ar^+ in a test configuration in which the collimator was biased to +8 kV and used to validate the collimator electro-optic model. Maximum transmission values of $\sim 2 \times 10^{-4}$ were obtained. This represents an upper bound to the actual ion transmission due to neutralization of a small fraction of the ion beam by charge exchange with the residual gas in the vacuum chamber; these neutrals can pass through the collimator and be detected.

If left exposed to the space environment, the collimator biased to +10 kV would attract and collect ambient electrons, including copious photoelectrons from the sunlit side of the spacecraft, resulting in a total electron current approaching 100 μA . Furthermore, many of these electrons would transit the collimator and ionize the residual gas in the space between the collimator and charge conversion subsystem; these ionized atoms and molecules would then be accelerated to the conversion foil and could masquerade as legitimate ENAs. To avoid both effects, negatively biased electron repeller ring electrodes are placed in front of the inner and outer radii of the collimator but completely outside of the collimator FOV. Figure 7 shows a cut through the entrance subsystem with simulated equipotential lines. To achieve a closed potential surface of -0.6 kV in front of the +10 kV collimator, the electron repeller electrodes are biased to -3.125 kV. Tests with an electron beam and the collimator biased to +10 kV demonstrated that rejection of electrons up to 0.6 keV is achieved with this configuration. We note also that photoelectrons and secondary electrons emitted from the electron repeller electrodes are accelerated to the collimator but only at high incident

Fig. 6 Transmission of 7.5 keV Ar^+ as a function of the azimuthal angle around the annular collimator entrance. The collimator is biased to +8 kV and the electron repeller electrode is biased to -2.5 kV. A radial spoke spanning the aperture at 0° completely blocks the incident beam. Except for measurements at the spoke, these measured transmission values represent an upper limit because of the small fraction of Ar^0 in the incident beam that passes through the collimator and is detected

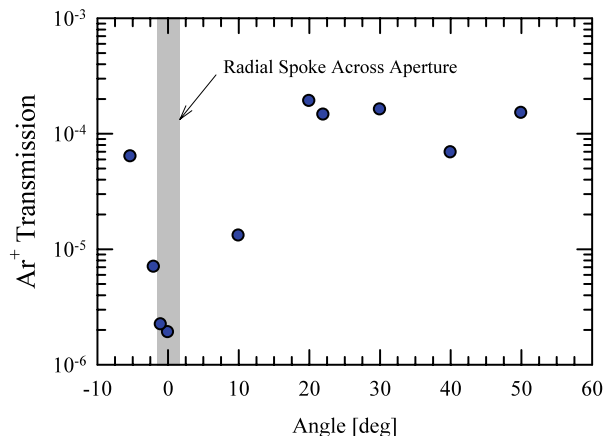
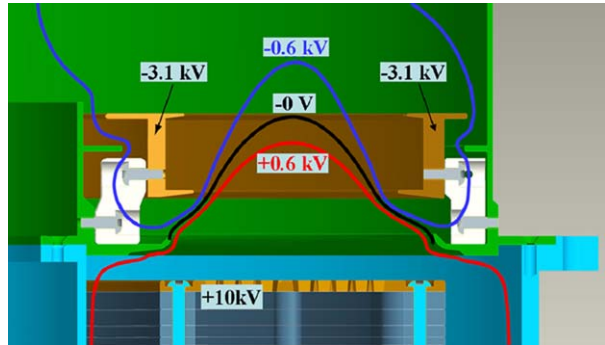


Fig. 7 The radial cut through the IBEX entrance subsystem illustrates equipotential field lines based on the subsystem's SIMION electro-optic model. When the collimator and electron repeller electrodes are biased to +10 kV and -3.1 kV, respectively, a closed -0.6 kV equipotential surface spans the entrance region, thereby rejecting all electrons with energies ≤ 0.6 keV



angles significantly outside of the collimator FOV, thus preventing these electrons from reaching the critical volume between the back of the collimator and the charge conversion subsystem.

2.2 Charge Conversion Subsystem: ENA Ionization

ENAs that transit the collimator enter the charge conversion subsystem whose purpose is to convert the ENAs to positive ions by transmission through an ultrathin foil. A total of 15 foils are distributed in a circular array as shown in Fig. 8 with inner and outer radii of 14.41 cm and 16.56 cm, respectively. These foils are nominal $0.6 \mu\text{g cm}^{-2}$ carbon from ACF Metals and are mounted on 333 line-per-inch (lpi) Ni grids that have a typical transmission of 73.4% as measured using a 50 keV H^+ beam. Each foil is mounted on a two-window foil frame that was determined by analysis and testing to be the optimal geometry for acoustic survival during launch. The foil frames each have an open area of 10.44 cm^2 for a total conversion foil area of 156.6 cm^2 . The conversion foil grid transmission was measured to be 73.4%, and the transmission of the photoelectron suppression grid located immediately in front of the conversion foils was 95%.

The probability of H^0 exiting the foil as H^+ is shown in Fig. 9 (Funsten et al. 2001). The ionization probability ranges from 0.013 at 0.33 keV to 0.13 at 6 keV, and the laboratory data infer two different ionization regimes by their different energy dependence. ENAs also lose energy in the foil as measured by Allegrini et al. (2006).

The foil constant $k_F = E_0 \psi_{1/2}$, in which E_0 is the energy of an incident H^+ ion beam and $\psi_{1/2}$ is the angular halfwidth of the scattered beam after transit through the foil, was measured for each foil as a proxy for foil thickness (Funsten et al. 1993) and to quantify its energy-dependent angular scattering, which is an important part of the end-to-end sensor model. The angular halfwidth $\psi_{1/2}$ was determined by integrating the 2-D scatter distribution in one (x, y) dimension and dividing by 1.19 to correct for integration of a Lorentzian distribution. The measured foil constant, frame serial number, and location in IBEX-Hi of each foil are listed in Table 2. The average foil constant for all foils is 18.5 keV deg. The foils were additionally analyzed for pinholes using Ar^+ beam analysis (Funsten et al. 1992), and the pinhole fraction was less than 1% for all foils.

One possible source of significant background is electron impact ionization of outgassing atoms and molecules in the region between the conversion foils, which lie at ground potential, and the collimator, which lies at +10 kV. Ionization is caused by photoelectrons or secondary electrons that are emitted from the entrance surface of a foil or a foil frame surface and then accelerated toward the collimator. Ionized atoms and molecules are accelerated in

Fig. 8 The charge conversion foil locations are noted in this front view of the IBEX-Hi sensor that has its entrance subsystem, ESA subsystem, and detector cover removed

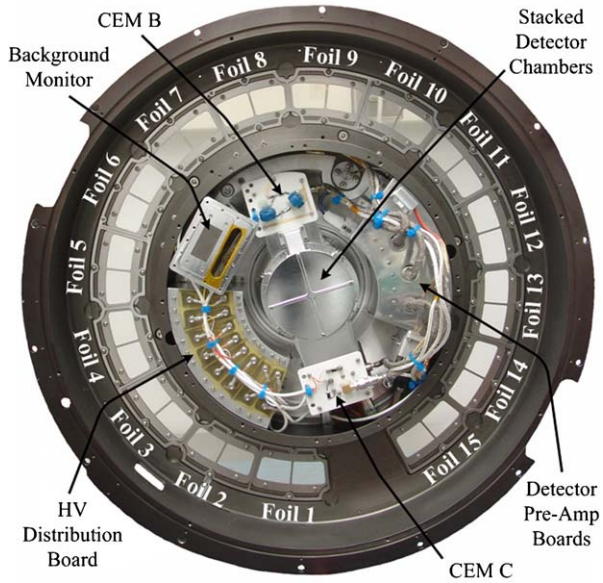
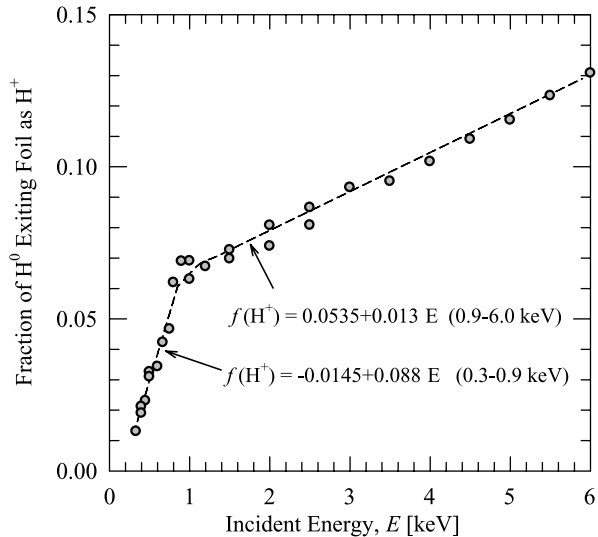


Fig. 9 The measured ionization probability of H^0 transmitted through an ultrathin carbon is shown as a function of incident energy



the opposite direction of electron acceleration, directly toward the conversion foils. These ions could exit the foil within the energy range of IBEX-Hi, therefore masquerading as heliospheric ENAs. We have minimized this “ion gun effect” background in two ways. First, the charge conversion foils act as a seal to block gas in the energy analysis and detector subsystems from entering the collimator region, which minimizes the pressure of the ambient gas in the “ion gun” region. Second, the charge conversion subsystem incorporates a 25 lpi nickel grid with 95% transmission located 0.48 cm in front of the charge conversion foils and biased to -300 V to suppress the photoelectrons and secondary electrons. Simulations show complete suppression of photoelectrons and secondary electrons emitted from

Table 2 IBEX-Hi foil placement and measured foil constant k_F . The requirement for IBEX-Hi is $k_F \leq 25$ keV deg

Foil location	Foil number	Foil constant, k_F [keV deg]
1	27	16.8
2	30	19.3
3	19	19.3
4	31	16.8
5	42	20.2
6	43	17.6
7	17	18.5
8	38	18.5
9	41	18.5
10	48	18.5
11	33	19.3
12	49	16.8
13	40	20.2
14	36	19.3
15	50	16.8
Average		18.4

the conversion foils and foil frames with energies up to at least 30 eV; this value is significantly lower than might be expected from a -300 V grid bias because of the large field leakage due to the high geometrical grid transmission (Read et al. 1998). The suppression grid reduces the “ion gun” background by a factor of ~ 20 .

2.3 Energy Analysis Subsystem

Positively ionized ENAs exiting the charge conversion foil enter the electrostatic energy analyzer (ESA), whose inner and outer analyzer plates are shaped like a “Bundt” baking pan (Moestue 1973). This geometry was successfully used on the Russian Interball mission (Vaisberg et al. 1995) and on the ISTP/POLAR mission (Shelley et al. 1995). The radius of the electro-optic surface of the inner (outer) ESA plate is 5.32 cm (8.34 cm), with the center of this radius located 8.76 cm (8.83 cm) from the central symmetry axis of the ESA plates and 0.82 cm (1.15 cm) below the plane of the conversion foils.

The inner ESA plate can be biased up to -7 kV and is the primary control for the central energy of each of the six energy passbands of IBEX-Hi, where we define the central energy as the energy of the maximum of the sensor response function for the passband. The ESA plates had serrations of hemispherical troughs of radius 0.76 mm machined such that the troughs are concentric relative to the symmetry axis of the sensor and, therefore, are aligned perpendicular to the direction of electrostatic deflection of ionized ENAs in the ESA. The serrations minimize scattering of many background particles into the detector subsystem, including UV light, ENAs exiting the foil as neutrals, ionized ENAs outside of the set energy passband, and ions > 10 keV that can successfully transit the entrance and charge conversion subsystems.

The outer ESA plate is biased to -90 V, -80 V, and -20 V for the lowest three energy passbands (passbands 1, 2, and 3, respectively) for two purposes, both of which increase the energy analysis subsystem throughput. First, ENAs scatter in the foil, especially at lower energies, to an angle at which they cannot transit the ESA even though their energy resides

within the energy passband. For the lowest energy passband, the -90 V on the outer ESA plate coupled with the -780 V on the inner ESA plate accelerate and proximity focus ionized ENAs so they have a higher probability of transiting the ESA. Second, ENAs lose proportionately more energy in the foil at lower energies, so fewer ENAs that would otherwise transit the ESA actually do. Because all ionized ENAs are accelerated by the same energy into the ESA, they are subsequently analyzed at a higher central energy and, importantly, at a broader energy passband. This shift of ionized ENAs to higher energies in the ESA and the wider energy passband at these higher energies therefore enable a higher throughput to compensate for the larger energy loss in the foil at lower incident ENA energies.

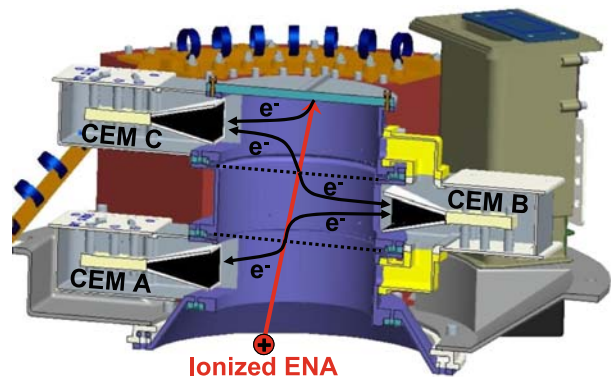
The intrinsic geometry of the toroidal ESA plates provides azimuthal focusing throughout the first 90° of deflection and azimuthal defocusing beyond 90° . The detector subsystem is biased to -6 kV to accelerate ionized ENAs into the detector subsystem to counteract this defocusing and also to increase the detection efficiency of the ionized ENAs. Electro-optic simulations of the coupled ESA and detector subsystems optimized the design so that the focal points of ENA trajectories at the central energy of each passband are located near the center of the detector subsystem and along its central axis.

2.4 Detector Subsystem

The detector subsystem consists of three nearly identical, stacked cylindrical chambers, each 5.6 cm in diameter and 2.6 cm tall and each having a CEM detector as shown in Fig. 10. The chambers, designated A, B, and C as sequentially encountered by an ionized ENA, are separated by two thin (nominal $2 \mu\text{g}/\text{cm}^2$) carbon foils (McComas et al. 2004). The ionized ENAs transit the foils and generate secondary electrons (e.g., Ritzau and Baragiola 1998; Allegrini et al. 2003) at their entrance and exit surfaces. Similarly, the ionized ENAs generate secondary electrons when they impact the aluminum interior walls of the chambers or the back wall of Chamber C. As shown in Fig. 10 secondary electrons generated within one chamber are electrostatically attracted towards the CEM detector of the same chamber by the potential difference between the CEM funnel (-1.7 kV) and the chamber (-6.0 kV). The secondary electrons subsequently generate a pulse in the CEM, and detection of pulses in more than one CEM detector within a prescribed time window is registered as a coincident event.

Penetrating radiation (e.g., >5 MeV electrons or >100 keV photons) can generate a coincidence signal that can be mistaken for a detected heliospheric ENA. To minimize this effect, the CEMs are positioned so that no straight penetrating particle trajectory can go

Fig. 10 Ionized ENAs enter the IBEX-Hi detector subsystem and generate secondary electrons (e^-) at interior chamber surfaces including the foils between Chambers A and B and between Chambers B and C. These secondary electrons are detected in each chamber, enabling double (two chamber) or triple (three chamber) coincidence detection of a single ENA



through all three CEMs. Thus, a triple coincidence is limited to penetrating particles actually crossing the two carbon foils. Careful characterization of the background in the detectors and detector subsystem is described in Sect. 4 (Calibration and Performance) and in more detail in Wurz et al. (2009).

The Sjets CEMs have a rectangular funnel with a sensitive area of 1.20×2.47 cm. The carbon foils, procured from ACF Metals, are mounted on electro-formed 200 lpi nickel grids with a transmission of $\sim 78\%$. The entrance grid of Chamber A is covered by a 70 lpi electroformed nickel grid, with a transmission of $\sim 90\%$ but no foil.

When a secondary electron is detected by any of the three CEM detectors, short (3 ns) and long (96 ns) electronic coincidence windows are opened. During these intervals the electronics are triggered to accept and record events detected in the other CEMs. At the end of the long coincidence window, 18 unique combinations of events are possible. We note that an ionized ENA may not be detected for at least three reasons: the secondary electron yield from carbon foils is statistical (Poisson) with the non-zero probability that no secondary electron is produced (Gruntman et al. 1990); the electro-optic model shows that not all secondary electrons impact the sensitive area of the CEM detector; and the CEM detection efficiency for electrons at ~ 4 keV is ~ 70 – 80% (Paschmann et al. 1970).

The shortest travel time for a 6 keV ENA to traverse the two foils of the detector subsystem is about 17 ns, which is much longer than the short coincidence window duration of 3 ns. Because an ionized ENA enters Chamber A first and reaches Chamber C last, a coincident event with CEM C registering a pulse in the short time window when an event in CEM A is also detected is unlikely to be a real ENA. Therefore, we developed two qualification schemes, discussed in the next section, to prioritize coincidence combinations that are most likely associated with ENAs rather than penetrating radiation or accidental coincidences.

2.5 Electronics

The IBEX-Hi electronics are designed to capture coincident events between any of the three CEM detectors and to record counts from the CEM detector in the IBEX Ion Background Monitor (IBaM) (Allegrini et al. 2009, this issue). The electronics are distributed between the Combined Electronics Unit (CEU) and the IBEX-Hi sensor. Within the IBEX-Hi sensor, high voltage filters eliminate noise and charge amplifier electronics convert CEM charge outputs into digital signals for processing on the Digital Board in the CEU.

The CEU also contains the high voltage power supplies (HVPS) for both sensors that generate and control voltages for the CEM detectors, collimator electrodes, and electro-optic elements. While the HVPS for both IBEX-Lo and IBEX-Hi reside on the same CEU board, their physical layouts are completely separated so that a fault on the HVPS of one sensor will not affect the HVPS performance of the other. The IBEX-Hi HVPS, their maximum and nominal operating voltages, and maximum output currents are listed in Table 3. Except for the Collimator (+) voltage, the high voltages for IBEX-Hi are generated by linearly regulating the output voltage from bulk high voltage supplies, which increases the overall efficiency. The step settling time of the inner ESA plate supply is 0.2 s for a step from -7.0 kV to -0.5 kV and 0.05 s for a step from -0.5 kV to -7.0 kV, both of which are much shorter than the measurement time at a single energy step of two consecutive spacecraft spins.

The high voltages applied to the CEM detectors and the chamber stack are filtered to prevent the introduction of noise in the signal electronics. Each CEM detector has a one-pole low-pass filter with a cut-off frequency of 72 Hz. The coaxial return line for each CEM HVPS has a “zap-trap” of back-to-back diodes and a capacitor to provide a chassis

Table 3 IBEX-Hi high voltage power supplies (HVPS)

High voltage power supply	Max. voltage (kV)	Nominal operating voltage (kV)	Max. current (μ A)
Collimator (+)	11.0	10.0	4
Collimator (-)	-4.6	-3.1	4
CEM_A	-4.6	-1.7	23
CEM_B	-4.6	-1.7	23
CEM_C	-4.6	-1.7	23
CEM_D	-4.6	-1.7	23
Detector	-6.0	-6.0	1
Chambers			
Inner ESA	-7.0	Energy dependent	1
Outer ESA	-0.30	Energy dependent	1
Suppression Grid	-0.30	-0.30	1

return path to dissipate the large filter capacitor in the event of a high voltage discharge, thus protecting the electronics within the sensor. The high voltage to the chamber stack uses a two-pole filter with a cut-off frequency of 127 Hz.

Amptek A121 fast hybrid charge amplifiers convert the electronic pulse outputs from the CEMs into digital pulses. The Amptek A121 was selected because of its relatively low power, voltage-adjustable threshold, and small package. The amplifier electronics were housed in separate, grounded enclosures for each CEM to maximize isolation and therefore minimize crosstalk between the CEMs' electronics chains. The anode output of each CEM is connected to the input of the charge amplifier by an RG-178 coaxial cable that is ~ 15 cm long. The charge amplifier is protected from high voltage discharge by a 100Ω carbon-composition resistor that is mounted away from other board components and followed by back-to-back input protection diodes.

The threshold for the A121 is voltage controllable within the range 5×10^4 – 5×10^6 electrons and commanded through software at a nominal operating value of 3×10^5 electrons. This is well above the analog noise floor, ensuring that no electronic noise can trigger a false coincidence in the measurement, and well below the centroid of the CEM pulse height distribution, ensuring no loss of valid counts. A filtered, differential-receive circuit processes the analog threshold that is generated in the CEU, reducing noise and re-referencing the threshold to the charge amplifier's ground. The output pulse width is set to 75 ns. The dead-time is 525 ns, implying a maximum theoretical periodic throughput for each channel of 1.9 MHz.

The TTL-level output of the charge amplifier is converted to Low Voltage Differential Signal (LVDS) levels before being transmitted to the CEU. This current-steering output produces small voltage swings that are equal and opposite, which minimizes noise on the power and ground lines. This is an important feature which greatly reduces the possibility of cross-talk between channels as well as feedback into the front-end of the amplifiers.

Besides the three CEM detectors (A, B, and C) in the IBEX-Hi detector subsystem, a fourth CEM detector (D) is used in the IBaM. CEM D plays no role in the coincidence measurement and simply accumulates counts to measure the ion background. The detector type

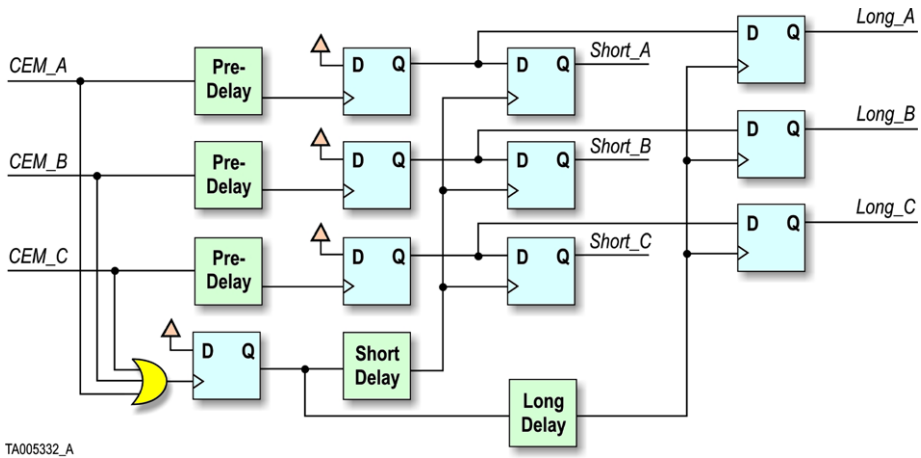


Fig. 11 The coincidence circuit within the CEU FPGA provides a novel polling scheme for capturing whether an event was detected in any of the three CEM detectors at the end of short and long time windows

and analog electronics (including input filtering, zap-trap protection, and charge amplifier board) for CEM D are identical to the other CEM detectors.

Test pulsers enable testing and exercising of the charge amplifier channels and the downstream coincidence circuitry. Each test pulse is equivalent to a CEM pulse magnitude of 6.8×10^6 electrons. The test pulsers are controlled by registers within the CEU field programmable gate array (FPGA). Various pulse patterns and coarse time delays can be generated to simulate all possible coincidence event types, providing tremendous flexibility to test the electronics chain.

The CEU receives the digital signals from CEM detectors A, B, and C and uses a novel polling scheme at the ends of two time windows to classify coincident events rather than more traditional and much more complex time-of-flight (TOF) measurement. As shown in Fig. 11, the digital signals from each CEM are split. The first lines are each input into a 4 ns fixed pre-delay and subsequently into a gated D-latch. When a pulse is detected in any CEM, its individual state is latched “hi” for the duration of the coincidence measurement.

The second lines split from the CEMs are used to poll the state of each CEM at two prescribed times (designated as “short” and “long”) using the following method. The CEM outputs are input into an OR gate to register if any CEM detected an event, and the output of the OR gate is latched for the duration of the coincidence measurement. The latch output is then split and input into a “short” time delay (controllable within a range of 1–8 ns in steps of 1 ns) and a “long” time delay (controllable within a range of 30–100 ns in 10 ns steps). The outputs of the time delays are used as the clock inputs, or triggers, for the final gated D-latches to record snapshots of which detectors register an event at the ends of the short and long time windows. The contribution of the pre-delay of 4 ns combined with the nominal (but adjustable) settings for the short and long time delays of 7 ns and 100 ns, respectively, correspond to nominal short and long coincidence windows of 3 ns and 96 ns, respectively.

When an event is detected, the latched outputs of Short_A, Short_B, and Short_C are registered at the end of the short time window, and the latched outputs of Long_A, Long_B, and Long_C are registered at the end of the long time window. If a latched state is “hi”, which corresponds to a detected event, then this state is recorded for the appropriate time window and detector. A “hi” event state captured at the end of the short window is designated as

lowercase “a”, “b”, or “c” and at the end of the long window is designated as uppercase “A”, “B”, or “C” according to the CEM detector in which the event occurred. Note that an event registered in the short window will also be registered in the long window.

We define a “Long” event as any non-coincident or coincident event that has registered at least one “hi” state at the end of the long time window, irrespective of whether it was registered as a “hi” in the short time window. The set of Long events therefore includes all single events and coincidence combinations. For example, a “Long AB” corresponds to all possible coincident AB events: aAB, bAB, and abAB.

Because an ionized ENA sequentially traverses Chambers A, B, and C, we find that some coincidence combinations more likely result from detection of ENAs, such as an A event first observed in the short time window and a C event only observed in the long time window. Conversely, other combinations more likely result from penetrating radiation, such as both A and C events detected in the short time window. Therefore, IBEX-Hi has two qualification schemes, either of which can be invoked by the CEU for any coincidence combination, to prioritize individual coincident events for the histogram data and the direct event data stream.

The first qualification scheme, denoted as Qual(Not_C), retains all coincident events of a coincidence combination in which the short time window never includes an event in Detector C. For example, “Qual(Not_C) ABC” retains only the triple coincidence events aABC, abABC, and bABC.

The second qualification scheme, denoted as Qual(Not_Equal), retains all events in which the events in the short and long windows are different. For triple coincidences, “Qual(Not_Equal) ABC” includes all triple coincidence events except for abcABC; in another example, “Qual(Not_Equal) AB” includes aAB and bAB but excludes abAB.

We note two additional features of this implementation. First, the pre-delay of 4 ns mentioned above combined with the adjustable short time delay provides a trim range to set a short coincidence window that includes 0 ns and record a snap-shot of the combination of CEM signals that caused the event to start. Second, the coincidence measurement can statistically identify and quantify the abundance of heavy ions in the measurement (Allegrini et al. 2008).

3 Sensor Model

An end-to-end performance model of IBEX-Hi was developed and refined throughout development of the sensor to optimize the sensor design and to simulate and evaluate performance of the subsystems individually and the sensor as a whole. The model is constructed with a combination of analytic modeling, electro-optic simulations, and physics modeling of specific sensor elements. Electro-optic design and simulations were performed using SIMION, a commercially available charged-particle optics simulation package (Dahl 2000).

Testing of IBEX-Hi subsystems and calibration of the fully assembled sensor has been used to validate most components of this model. The calibration results alone do not constitute a complete characterization of IBEX-Hi; in fact, only a limited subset of all possible ion or neutral atom energies, species (H and O), incident angles, and foil locations on the sensor could be tested in the time available. A high-fidelity sensor model allows us to interpolate between these data points to derive an integrated response function and to predict sensor response across the full possible range of operational conditions expected throughout the mission, allowing the flexibility to modify the measurement strategy if needed for discovery science.

The end-to-end model includes a geometric ray-tracing of the collimator, an empirical determination of foil transmission and ionization fraction, and 3-D electro-optic SIMION models of the energy analysis and detector subsystems. The end-to-end simulation is performed by propagating a large number ($N \sim 10^6$) of ENAs distributed in energy (E) and angle (θ, ϕ) through the model for each of the 6 energy settings (j) of the ESA. As the ENAs “fly” through each sensor element (k), they are appropriately propagated in a manner that reflects the physical action of that particular element. At each stage, the transmission efficiency ($T_{j,k} = N_{j,k}^{\text{out}}/N_{j,k}^{\text{in}}$) is determined. Note that T , N^{in} , and N^{out} are all functions of energy, angle, and position. We consider each stage in turn below.

Collimator As previously described, the IBEX-Hi collimator is composed of a stacked array of hexagonal cells that restrict the FOV to 6.5° FWHM. Because the FOV is based solely on the geometry of a hexagonal channel, the angular dependence of the collimator transmission is accurately modeled using the collimator response function $P(\theta, \phi)$, which is illustrated in Fig. 4 and is indistinguishable from the measured performance. The sensor simulation is initiated here, with virtual ENAs uniformly spread across the cell entrance and uniformly distributed in angle up to $\pm 10^\circ$ relative to the collimator boresight.

Conversion Foil Ultrathin carbon foils are used to convert a fraction of the incident ENAs into positive ions that are then energy-analyzed and accelerated into the detector section. Although the desired function of the foil is to simply strip an electron from an ENA, the ENA also undergoes statistical processes of angular scattering, energy loss, and ionization. These are simulated via Monte-Carlo sampling of energy-dependent empirical functions for each of the above factors.

- The scattering angle for a given ENA is determined by sampling a 2-D Lorentzian-squared, having an angular width determined by the ENA’s initial energy and laboratory measurement of the foil constant k_F . The use of a Lorentzian-squared is based on empirical best fit to the measured laboratory distribution.
- Energy loss of ENAs at energies > 1 keV is based on measurements by Allegrini et al. (2006) and uses an asymmetric Gaussian energy distribution having a mean and width that are functions of foil thickness, ion species, and ion energy. These results were extrapolated for ENA energies < 1 keV.
- The probability for ENA transmission through the foil τ_{Foil} was derived using SRIM (Ziegler et al. 1985) Monte-Carlo simulations of protons incident on a $1.7 \mu\text{g cm}^{-2}$ carbon foil. The results were fit to $\tau_{\text{Foil}} = \exp(-9.594 \times 10^4/E^2)$, where E is in eV.
- The probability of an ENA exiting the foil as H^+ is determined from the formulas in Fig. 9.

Electrostatic Energy Analyzer (ESA) A SIMION electro-optic model of the energy analysis subsystem incorporates the geometry of all relevant electrostatic elements, and the trajectories of H^+ exiting the foil through the ESA are subsequently computed. Figure 12 compares the simulation and calibration (Cal 1) results of the absolute transmission of the combined conversion foil and ESA for each of the six energy steps. The model clearly reproduces the measured behavior, including the energy passband centers and widths, especially for the higher energy passbands. The good correspondence, which is slightly worse at lower energies where the conversion foil behavior is less well known, gives us confidence in our general understanding of the foil physics and ESA electro-optics. We have employed a scaling factor to the modeled transmission values to account for the differences between the simulations and the calibration data; the scaling factors range from 1.45 at energy step 1 to 0.88 at energy step 6.

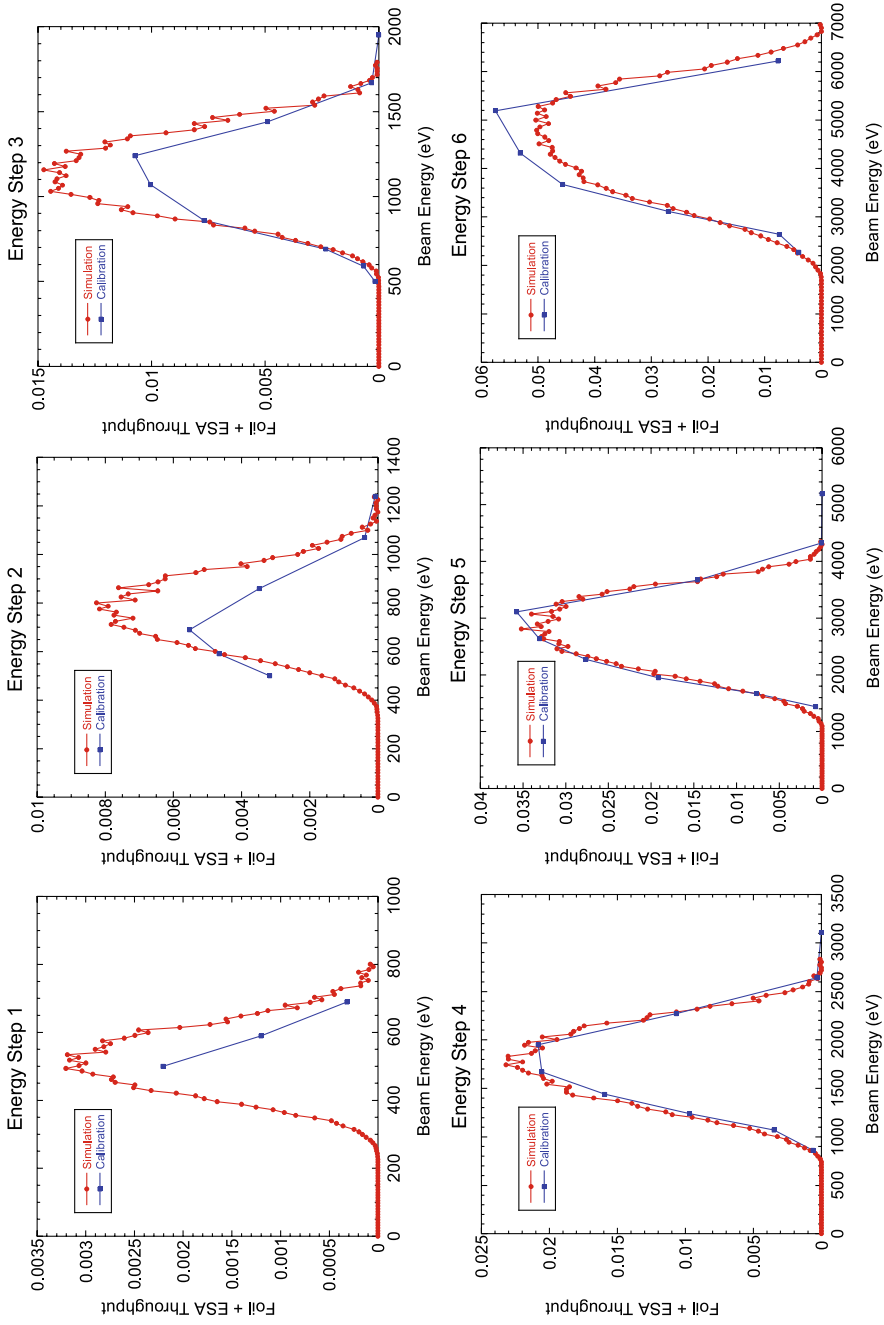


Fig. 12 Comparison of simulations and Cal 1 measurements of the absolute transmission of the combined charge conversion and energy analysis subsystems. Agreement is generally good, although slightly worse at lower energies where the conversion foil behavior is less well known

Detector Subsystem The detector model uses a separate electro-optic model for each chamber and a single carbon foil model for the foils between Chambers A and B and Chambers B and C. Simulated H^+ ions are initially incident at the entrance grid of Chamber A and sequentially propagate through the electro-optic model of Chamber A, the foil model, the electro-optic model of Chamber B, the foil model, and finally the electro-optic model for Chamber C. At the location of ion impact on each foil, the probability for secondary electron emission from each surface is calculated using a Poisson distribution and the measurements of Kozochkina et al. (1993) and Ritzau and Baragiola (1998). These secondary electrons, in turn, are propagated through the appropriate chamber electro-optic model by following their trajectory to the CEM detector, and their detection probability is 0.7. The detector represents the most complex and uncertain component of the end-to-end model, and at the time of the IBEX launch the sensor response function is primarily based on the empirical, scaled detector response that is discussed in Sect. 4 (Calibration and Performance).

4 Calibration and Performance

IBEX-Hi had four phases of calibration: Cal 1, which included calibration without the collimator and photoelectron suppression grids for quantification and electro-optic validation of the integrated performance of the charge conversion and energy analysis subsystems with ion and neutral atom beams; Cal 2, which verified performance for a small subset of energies and foils and was performed between vibration testing and thermal-vacuum testing (Jones and Bernardin 2007); Cal 3, which used the spare CEU that was functionally identical to the flight CEU for detailed, end-to-end performance characterization; and Cal 4, which was cross calibration with IBEX-Lo.

Cals 1, 2, and 3 were performed at Los Alamos National Laboratory (LANL) using a magnetically mass-resolved H^+ beam generated by a microwave ion source having an intrinsic energy spread <2 eV and accelerated to an energy from 0.45 to >10 keV. A neutral hydrogen (H^0) beam was created by charge exchange of the H^+ beam with the residual gas in the beam line between the mass-analyzing magnet and the calibration chamber, and the remaining H^+ in the H^0 beam was magnetically deflected before it could enter the chamber. The beam transited a 2.0-mm-diameter aperture and had a measured diameter at the IBEX-Hi entrance of ~ 2.2 mm for energies ≥ 1 keV and 2.8 mm at 450 eV. The wider beam at the sensor entrance was due to angular divergence of the beam. The typical chamber pressure was $\leq 2 \times 10^{-7}$ torr, and Residual Gas Analysis (RGA) spectra were obtained at least once each day and every 20 minutes when IBEX was under vacuum but not powered. Cal 4 was performed at SwRI; details of the SwRI calibration facility are provided in McComas et al. (2009a).

In all calibrations, the ion or neutral atom beam flux was measured using an absolute beam flux monitor that is schematically illustrated in Fig. 13. The monitor utilizes a coincidence scheme (Funsten et al. 2005) in which an ion or neutral atom beam generates secondary electrons at the entrance surface of a foil, and these electrons are accelerated to and detected by detector D1. A fraction of the beam transits the foil and generates secondary electrons on the back surface of the foil and at the back plate of the monitor; these secondary electrons are accelerated toward and registered by detector D2. The absolute detection efficiencies for each detector are derived from measurement of the single (non-coincident) count rates C_1 and C_2 of CEM detectors D1 and D2, respectively, and the coincidence count rate C_{COIN} between them. The probability (and therefore detection efficiency) that an ion that enters the monitor is detected by D1 is $\varepsilon_1 = C_{\text{COIN}}/(C_{\text{COIN}} + C_2)$. Similarly, the D2 detection efficiency is $\varepsilon_2 = C_{\text{COIN}}/(C_{\text{COIN}} + C_1)$. Because these detection efficiencies include

Fig. 13 The absolute beam flux monitor was used to measure the H^+ or H^0 beam flux throughout the IBEX-Hi calibrations

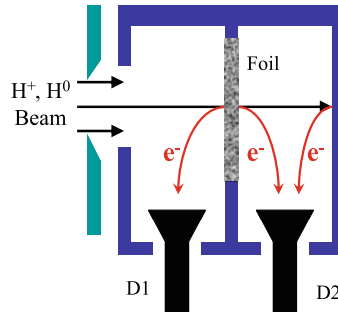


Table 4 Average background count rates for exclusive (non-coincident) single events and a subset of coincidence types measured over 19.6 hours of quiescent operation during cross calibration

Measurement		Background rate
Singles	CEM A	89 mHz
	CEM B	115 mHz
	CEM C	69 mHz
	CEM D	12 mHz
Double coincidences	Long AB	2.8 mHz
	Long BC	4.2 mHz
	Qual(Not_C) AC	0.13 mHz
Triple coincidences	Qual(Not_C) ABC	0.58 mHz
	Long ABC	1.04 mHz

the secondary electron yields, the fraction of the beam that transits the grid-mounted foil, and the probabilities that secondary electrons are accelerated into the detectors and generate pulses, we do not need to know these quantities individually. The resulting coincidence efficiency is therefore $\epsilon_{\text{COIN}} = \epsilon_1 \epsilon_2$, and the incident beam flux is therefore $C_{\text{COIN}} / (A_B \epsilon_{\text{COIN}})$, where A_B is the cross-sectional area of the beam.

The beam flux and beam stability were measured throughout the calibrations. The stability was typically 1–3% over a single IBEX-Hi measurement. The beam was also monitored for drift over time, and typical drift for >80% of the calibration data was $\leq 5\%$. Importantly, the IBEX-Hi sensor telemetry stream reports single (non-coincident) count rates for each of its three detectors as well as all coincidence count rates, enabling *in situ* monitoring of detection efficiencies of each detection chamber throughout the IBEX mission using this method.

The average background count rates, listed in Table 4, were measured over 19.6 hours during Cal 4 (cross calibration) when the sensor was fully operational but had no incident ion or ENA beam. The singles count rates in each CEM detector were < 0.2 Hz. While the coincidence count rates are higher than expected based on random coincidence of the background singles rates in the detectors, we have found that ambient gamma rays are associated with a majority of the background coincidence events observed in the detector subsystem. This is based on the relative frequency of different coincidence combinations in the detector subsystem from a ^{137}Cs source placed next to the sensor, from a 3.5 keV H^+ beam, and under a quiescent (unstimulated) condition. We used laboratory TOF electronics to measure the TOF between detected events in all coincidence combinations. While most coincident events from the 3.5 keV H^+ beam involved a first pulse from CEM A and no events in which

CEM C registered the first pulse, both the ^{137}Cs source and quiescent background generated approximately an equal number of coincidences in which CEM A and CEM C registered the first pulse. We note that ^{137}Cs also emits 1.175 MeV electrons that have a range of ~ 2.3 mm in Al, but these were completely blocked by the Al walls of minimum thickness >2.5 mm surrounding the interior of the detector chambers and CEM detectors.

We subsequently measured the background γ -ray environment in the LANL calibration facilities, showing a background flux of $6.3 \gamma \text{ cm}^{-2} \text{ s}^{-1}$ between 0.2–3 MeV and specific γ -ray lines corresponding to ^{40}K (K is used in concrete) and daughters associated with ^{222}Rn . Therefore, because a majority of coincident counts listed in Table 4 result from the ambient γ -ray environment of the calibration laboratory, the measured background count rates are significant overestimates of the background rates expected in space from this mechanism.

IBEX-Hi was also tested for response to UV light, in particular to study the “ion gun” effect in which photoelectrons generated at the conversion foil are accelerated toward the +10 kV collimator and ionize ambient atoms or molecules, which in turn are accelerated into the conversion foil and can masquerade as ENAs. During Cal 1, an Ar-purged deuterium lamp, followed by two notch filters used to maximize the fraction of H Ly α (1216 Å) and a MgF_2 window, directly illuminated the conversion foils. The photon rate at the foils was $\sim 4 \times 10^{10} \text{ s}^{-1}$ as measured using a calibrated UV photodiode (Korde et al. 2003). The ion gun effect was observed when the collimator was biased to +10 kV and no voltage was applied to the photoelectron suppression grid, yielding individual count rates in CEMs A, B, and C of 17, 12, and 1.6 Hz, respectively; a total double coincidence rate of ~ 0.1 Hz; and a total triple coincidence rate of <0.05 Hz. The double and triple coincidence rates dropped to background levels when the collimator voltage was switched from +10 kV to 0 V.

The IBEX-Hi FOV alignment was measured during Cals 1 and 3 using a theodolite located at a viewport at the rear of the calibration chamber, collinear with the beam axis, and boresighted with two beam-defining apertures upstream of the chamber. A double-sided mirror was mounted flush to the IBEX-Hi baseplate to an estimated accuracy of $<0.1^\circ$, and the alignment was measured using autocorrelation. The reproducibility of the autocorrelation and movement of the motion stages was $\leq 0.02^\circ$. Alignment accuracy of the theodolite with the upstream apertures is estimated to be $\sim 0.1^\circ$. Finally, angular divergence of the H^0 beam was measured to be 0.2° FWHM. Using this alignment scheme, the angular response of the sensor to a 2.7 keV H^0 beam incident on Foil 6a was measured at Energy Passband 5 at several points in the azimuthal and polar directions, and the results are shown in Fig. 14. An angular offset of $0.17 \pm 0.07^\circ$ in polar and $-0.20 \pm 0.07^\circ$ in azimuth is likely due to a combination of the tolerance errors mentioned above and possibly a slight angular dependence of the overall sensor response. After correcting for beam divergence, the collimator acceptance angle was measured to be $6.5 \pm 0.1^\circ$ FWHM, in agreement with the collimator tests described previously.

Using the Cal 1 results of the combined throughput of the conversion foils and energy steps as shown in Fig. 12, the central energies and energy resolutions were derived for double and triple coincidence events and are shown in Fig. 15. The FWHM energy resolution ranges from approximately 0.45 at the lowest energy passband to about 0.65 at the highest energy passband. Although limited to only the charge conversion and energy analysis subsystems (and therefore not representative of the flight energy passbands or the end-to-end IBEX-Hi energy response), this data was used to validate the physics model of the conversion foil and the electro-optic design of the ESA.

The energy-dependent trajectories through the ESA govern the location and angle at which an ionized ENA enters the detector subsystem. Furthermore, there is a known spatial dependence of the detection efficiency for each detector chamber because the CEM detectors

Fig. 14 The IBEX-Hi angular response as measured using a 2.7 keV H⁰ beam

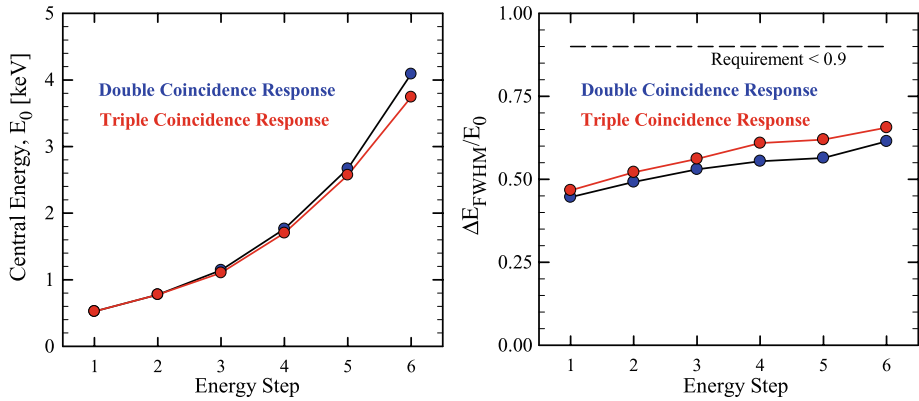
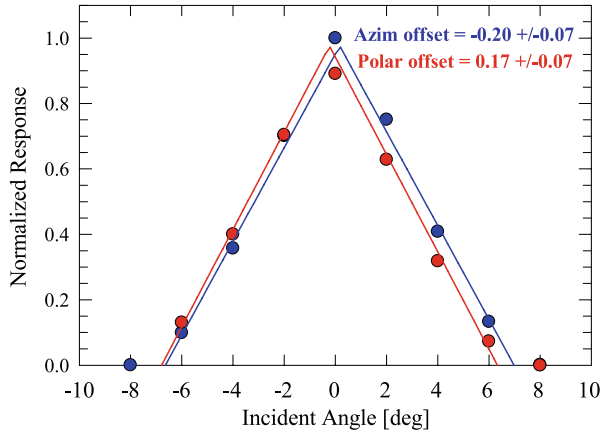
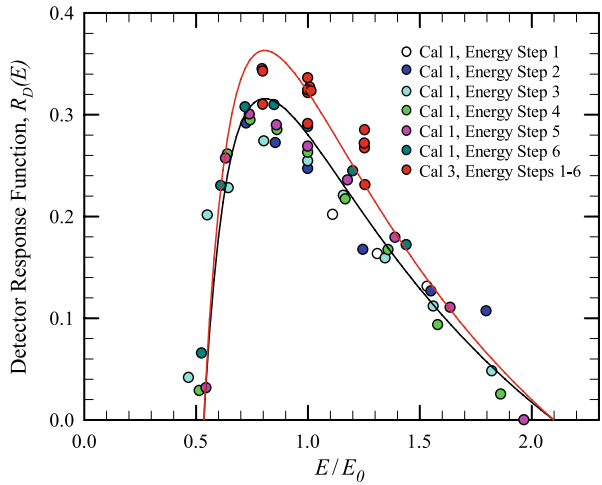


Fig. 15 The central energies (*left panel*) and energy resolutions (*right panel*) of the combined charge conversion and energy analysis subsystems are shown for each energy step as measured during Cal 1. Double coincidences are the sum of Long AB, Long BC, and Qual(Not_C) AC counts. Triple coincidences are Qual(Not_C) ABC counts

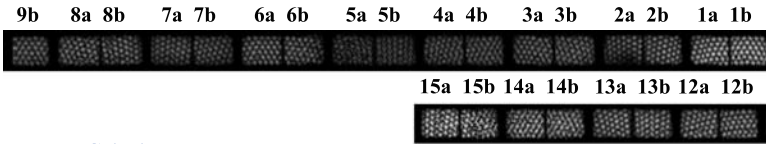
are located on one side of each chamber. However, because ionized ENAs are accelerated by 6 keV into the detector subsystem and because of the scalability of electro-optics, we expect that (1) the response for each energy passband can be generally scaled according to E/E_0 where E_0 is the central energy of the passband and E is the initial ENA energy and (2) the detection efficiency for the coincidence combinations are generally independent of energy. Figure 16 shows the detection efficiency for summed double coincidences (defined in the figure caption) as a function of E/E_0 for all passbands and all energies used during Cal 1 and Cal 3. The data for each coincidence combination were fit to $\varepsilon(E/E_0) = c_1 + c_2((E/E_0 + c_3) - c_4)^2$ where $c_1, c_2, c_3,$ and c_4 are fit parameters, and this empirical equation is used as the basis for the detector response in the end-to-end sensor model.

The Cal 3 results show a slightly higher efficiency of the detector subsystem, which likely resulted from new foils installed between Chambers A and B and Chambers B and C. These new foils were mounted using an improved technique and had a higher fraction of coverage over the support grid. To reflect this enhanced detection efficiency, the upper curve in Fig. 16

Fig. 16 The empirical detector subsystem response for all energy passbands for double coincidence events is approximately represented by a single equation. Cal 1 results are the sum of Long AB, Long BC and Long AC, whereas the Cal 3 results are the sum of Long AB, Long BC, and Qual(Not_C) AC. The *black line* is an empirical fit to the Cal 1 results, and the *red line* is the Cal 1 empirical equation scaled by a factor of 1.15 to fit the Cal 3 results



Singles (Non-coincident) Events



Double Coincidences



Triple Coincidences



Fig. 17 Response of the IBEX-Hi sensor to a beam of 2.8 keV H^0 , where the arc-shaped foil apertures have been flattened such that the horizontal direction corresponds to azimuth. Double coincidences are the sum of Long AB, Long BC, and Qual(Not_C) AC counts. Triple coincidences are Qual(Not_C) ABC counts

was derived by linear scaling of the empirical Cal 1 equation to the Cal 3 results, which were incorporated into the end-to-end sensor response function.

During Cal 3, a 2.8 keV H^0 beam was directed along a snake-like path at a steady rate of 1 mm/sec along a radial line across a foil and through 0.36° azimuthal steps between the radial lines. The incident beam flux was intermittently re-measured using the absolute beam current monitor to monitor beam flux drift. The relative singles (non-coincidence) rates, double coincidence rates, and triple coincidence rates over multiple foils is shown in Fig. 17, in which brighter pixels correspond to higher count rates. The response is observed to change as a function of azimuthal angle (horizontal direction in the figure). This response variation is the direct result of the azimuthal-dependent trajectories through Chambers A, B, and C and, in particular, the location of the CEM within each chamber. The axis of symmetry of the response observed in Fig. 17 and throughout IBEX-Hi calibrations lies along the line between CEM B (corresponding to the middle of Foil 8) and CEMs A and C (located between Foils 1 and 15). Table 5 shows the relative fraction of double and triple coincidence

Table 5 Relative probabilities of occurrence for different double and triple coincidence combinations. Note that coincidence combinations abcABC, acAC, cAC are not included because they are not likely produced by an ENA in the detector subsystem. CEM D is the detector in the IBaM

Triple coincidence event set	Combination	Event probability
Qual(Not_C) ABC	aABC	0.64
	bABC	0.14
	abABC	0.22
Double coincidence event set	Combination	Event probability
Long AB	aAB	0.18
	bAB	0.03
	abAB	0.06
Qual(Not_C) AC	aAC	0.08
Long BC	bBC	0.49
	cBC	0.07
	bcBC	0.09

events averaged over the energy passbands. The most probable triple and double coincidence events are aABC and bBC, respectively.

Calibration results were used to refine and validate all of the modeled and simulated components of the end-to-end sensor model except for the detector subsystem, which uses the empirical response shown in Fig. 16. The model is then used to interpolate the response for energies, foil locations, and incident angles not measured during calibration and derive the integrated response of the whole sensor. The count rate C_i of IBEX-Hi corresponding to an ENA flux of $J(E, \Omega) \text{ cm}^{-2} \text{ sr}^{-1} \text{ eV}^{-1} \text{ s}^{-1}$ at ESA setting i (with central energy E_i) is

$$C_i = \int J(E, \Omega) G_i(E, \Omega) d\Omega dE. \tag{1}$$

The geometric factor G_i is constructed by separating the collimator response $P(\Omega)$ from the comprehensive energy-dependent response $R_i(E)$ of the sensor after the collimator:

$$G_i(E, \Omega) = AT_C P(\Omega) R_i(E). \tag{2}$$

In this equation, A is the total aperture area of the charge conversion foils (156.6 cm^2) and T_C is the fractional area of the collimator consisting of open apertures (0.67). The point spread function $P(\Omega)$ describes the angular response of IBEX-Hi, which, to a high degree of accuracy, can be represented solely as the energy-independent collimator response shown in Fig. 4. Because the incident ENA flux is expected to be relatively constant over the solid angle of any single azimuthal pixel, the integrated collimator response corresponds to a solid angle of $\int P(\Omega) d\Omega = 0.0147 \text{ sr}$.

The sensor response function $R_i(E)$ describes the cumulative, energy-dependent response to ENAs that exit the collimator and are incident within the total area of the charge conversion foils. $R_i(E)$ therefore includes all factors governing transmission and transport through the charge conversion, energy analysis, and detector subsystems, as well as the probability of detection in each CEM chamber. The response function was generated using the end-to-end sensor model, and the results for double and triple coincident events are shown in Fig. 18. The primary uncertainty of the sensor response function lies in the empirical detector subsystem response function. Using the end-to-end response function, the flight energy passband settings have been defined as shown in Table 6.

Fig. 18 The response function $R_i(E)$ of the IBEX-Hi sensor is shown for each energy passband i . The double coincidence response includes the sum of Long AB, Long BC, and Qual(Not_C) AC events. The triple coincidence response corresponds to Qual(Not_C) ABC events

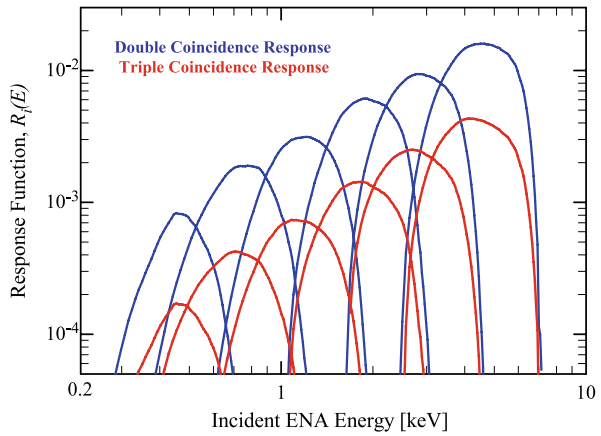


Table 6 Flight energy passbands for double and triple coincidence events as derived from the sensor end-to-end model for each of the six IBEX-Hi energy steps. The full-width-at-full-maximum values ($E_{+FW} - E_{-FW}$) represent the 99% level and central energy E_0 represents the energy of the maximum (peak) value of the response function

ESA setting			Double coincidences: Long AB + Long BC + Qual(Not_C) AC					
ESA Step	Outer ESA [keV]	Inner ESA [keV]	E_{-FW} [keV]	E_{-HW} [keV]	E_0 [keV]	E_{+HW} [keV]	E_{+FW} [keV]	$\Delta E/E_0$ [keV]
1	-0.09	-0.78	0.26	0.38	0.45	0.58	0.75	0.20
2	-0.08	-1.28	0.36	0.57	0.78	0.98	1.25	0.41
3	-0.02	-1.85	0.62	0.89	1.21	1.56	1.91	0.68
4	0	-2.88	1.07	1.45	1.92	2.53	3.02	1.08
5	0	-4.46	1.68	2.15	2.80	3.82	4.54	1.67
6	0	-7.00	2.57	3.34	4.51	6.14	6.93	2.80

ESA setting			Triple coincidences: Qual(Not_C) ABC					
ESA Step	Outer ESA [keV]	Inner ESA [keV]	E_{-FW} [keV]	E_{-HW} [keV]	E_0 [keV]	E_{+HW} [keV]	E_{+FW} [keV]	$\Delta E/E_0$ [keV]
1	-0.09	-0.78	0.24	0.38	0.45	0.59	0.75	0.47
2	-0.08	-1.28	0.35	0.52	0.71	0.95	1.23	0.60
3	-0.02	-1.85	0.58	0.84	1.08	1.55	1.93	0.65
4	0	-2.88	1.07	1.36	1.85	2.50	3.02	0.62
5	0	-4.46	1.68	1.99	2.70	3.75	4.54	0.65
6	0	-7.00	2.57	3.13	4.09	6.00	6.93	0.70

Based on simulations and recent estimates of ENA fluxes, the spectral slope of ENAs should sharply decrease with increasing energy above ~ 1 keV (e.g., Gruntman et al. 2001; Wurz et al. 2008). Therefore, derivation of the incident ENA flux $J(E, \Omega)$ from the sensor count rate C_i through inversion of (1) should be performed using an iterative, forward-modeling method. Nevertheless, the energy geometric factor, defined as

$$G_i^E = \frac{1}{E_i} \int G_i(E, \Omega) d\Omega dE, \tag{3}$$

Table 7 Values of the energy geometric factor G^E ($\text{cm}^2 \text{sr eV/eV}$) derived using (3) for the flight ESA passbands

ESA step	G^E , double coincidence: Long AB + Long BC + Qual(Not_C) AC	G^E , triple coincidence: Qual(Not_C) ABC
1	0.00060	0.00013
2	0.0016	0.00041
3	0.0028	0.00075
4	0.0053	0.0013
5	0.0086	0.0024
6	0.015	0.0045

can be used to estimate the ENA flux near energy E_i using $J(E_i) = C_i/E_i G_i^E$. The energy geometric factors for double and triple coincidence events are listed in Table 7 for each of the six IBEX-Hi energy passbands.

5 Sensor Operations and Data Handling

IBEX-Hi operates in science mode over the portion of the IBEX orbit when the spacecraft is above $15 R_E$, which is about 93% of the ~ 8 -day orbital period. In this mode, all high voltages are at nominal operating levels, and the ESA voltages are stepped once every two spacecraft spins. A complete energy sweep over all six passbands is therefore completed every 12 spins, which corresponds to 3 min based on a nominal spin rate of 4 rpm.

In science mode, IBEX-Hi reports two data products: (1) histograms of accumulated counts as a function of angle, energy step, and coincidence type, and (2) direct event data consisting of individual coincidence events selected using a prioritization scheme and reported at high time (and therefore angular) resolution. The telemetry rate is 42 bps for histogram data, 57 bps for direct event data, and 12 bps for housekeeping that is shared with IBEX-Lo.

Histograms are constructed from accumulated counts from coincident and non-coincident (single) events and sorted by event type. Each histogram is a 6×60 array of counts for the six energy passbands and 60 angular bins around the spin axis, each 6° wide. The angular bins of eight primary event type histograms are summed over four ESA cycles (12 minutes); another three secondary histograms are summed over eight ESA cycles. The counts in each angular bin are compressed from 16 bits to 8 bits and stored in the solid-state recorder (SSR) for downloading during the next IBEX perigee pass.

The primary histograms include non-coincident (singles) counts in each detector (Long A, Long B, Long C), four double coincident types (Long AB, Qual AB, Qual AC, and Qual BC), and one triple coincident type (Qual ABC). The secondary histograms include Long AC, Long BC, and Long ABC. The qualification scheme, either Not_C or Not_Equal, can be independently selected for each of the qualified coincidence event types. The histogram data also includes accumulated counts from the IBaM as a function of spin angle.

Direct event data consists of individual coincidence events whose coincidence type is reported along with the spin angle and energy passband at the time that the event was detected. Direct events are recorded at higher time resolution (4.2 ms, or $\sim 0.1^\circ$ of spin angle) than used for acquisition of the histograms. Because of telemetry constraints, IBEX-Hi is limited to recording ~ 800 direct events per 12-spin cycle, which corresponds to an average of ~ 67 events per spin. Therefore, a culling process is used by the CEU to telemeter only the

highest priority direct events. The prioritization scheme, which lies in a changeable look up table in the CEU, currently has Qual(Not_C) ABC as the highest priority because these triple coincidences represent the measurement with the lowest noise. These high priority events are stored up to the limit of ~ 800 events per 12 spins. If space remains, the second priority events, which currently include Long AB, Long BC, and Qual(Not_C) AC, are included in the direct event data. No other event types are stored as direct event data. Because direct events are recorded at greater time resolution and greater coincidence type specificity than the histograms (for example, the qualified-triples histogram includes three different types of direct events), they represent key data for deeper analysis of the global ENA maps.

IBEX-Hi has three other operational modes: high voltage standby mode, gain test mode, and functional test mode. High voltage standby mode is entered every orbit when the spacecraft passes below $15 R_E$ as it approaches the radiation belts. At these low altitudes, the magnetospheric ENA signal can be significantly greater than that of heliospheric ENAs, and detector background from penetrating radiation may also be substantial. Upon entering this mode, the collimator voltages are turned off, the voltage applied to the detector chambers is reduced from -6 kV to -4 kV, and the voltage across each CEM is decreased by 0.6 kV, which is below the threshold for electron avalanche in the CEM.

Gain tests are run periodically to ensure that the CEMs are operating on the plateaus of their respective gain curves. During a gain test, each CEM voltage is alternately stepped between its current operating voltage and offsets of -200 V, -100 V, $+100$ V and $+200$ V from operating voltage. Because the heliospheric ENA signal rate is quite low, gain tests are performed at $\sim 12 R_E$ to utilize the stronger magnetospheric ENA signal in some of the magnetospheric-viewing azimuthal pixels, resulting in anticipated ENA count rates of ~ 10 s $^{-1}$ in these pixels. Based on these count rates, the planned integration time per energy passband setting is ~ 12 minutes. The scheme of returning to the current operating voltage before proceeding to the next voltage offset minimizes the impact of natural fluctuations in the ENA rate on the test results. If a gain test shows that a CEM detector gain has decreased, the gain will be increased by an appropriate increase of the CEM operating voltage.

The electronics functional test is periodically executed to assess the health of the IBEX-Hi amplification and signal processing electronics. This is a shortened and automated version of the electronics checkout performed throughout calibration and during commissioning. Specific diagnostics include determination of the electronic noise floor discriminator setting and the lower level discriminator below which crosstalk between separate detectors is observed.

6 Summary

The IBEX-Hi imager is a sensitive, single pixel ENA imaging camera with a FOV of 6.5° with six contiguous energy passbands spanning an energy range of ~ 0.38 – 6 keV. Because of the anticipated tenuous signal at 1 AU of ENAs from the interaction region between the heliosphere and the LISM, the IBEX-Hi sensor design has been driven by maximizing sensitivity and minimizing background and noise, resulting in the most sensitive ENA sensor ever flown over its energy range. An end-to-end IBEX-Hi sensor performance model has been developed with most components validated through extensive testing and calibration. This model allows accurate quantification of the cumulative energy response and sensitivity of the sensor and enables the flexibility to modify instrument operations to optimize our measurement of new discoveries as they arise. The sensor meets the measurement requirements for acquiring global ENA maps that will allow us to answer the key scientific

questions regarding the structure and dynamics of the interaction between the heliosphere and the LISM. Although focused primarily on measurement of heliospheric ENAs, IBEX-Hi will also allow us to view and study regions of the terrestrial magnetosphere and possibly other planetary magnetospheres that have never been observed before in ENAs.

Acknowledgements The IBEX-Hi sensor is the result of an outstanding collaboration between scientists, engineers, technicians, and support personnel at multiple institutions, including Jeff Christmas and Lt. Brett Ryder of Air Force Research Lab (AFRL), Kirtland AFB; Charlie Briggs, Greg Ellison, Tracy Gerber, Marty Leahy, Charlotte Ogas, and Dan Wright of ATA Aerospace; Eric Stasiunas and Alex Pimatel at Sandia National Laboratories; Patsy Archuleta, Alan Baca, Sean Apgar, Randy Edwards, John Bernardin, and David Jones at Los Alamos National Laboratory (LANL); Chris Kofoed, Bob Harbaugh, Wendy Mills, Mike Young, Rob Ebert, Joe Westlake, Josh Alquiza, Tom Broiles, Brent Randol, and Roberto Livi at SwRI; and Georg Bodmer and Jürgen Scheer at the University of Bern. Work at Los Alamos National Laboratory was performed under the auspices of the United States Department of Energy.

References

- F. Allegrini, R.F. Wimmer-Schweingruber, P. Wurz, P. Bochsler, Measurement of the ion-induced electron yields from thin carbon foils for low energy ions. *Nucl. Instr. Meth. B* **211**, 487 (2003)
- F. Allegrini, D.J. McComas, D.T. Young, J.-J. Berthelier, J. Covinhes, J.-M. Illiano, J.-F. Riou, H.O. Funsten, R.W. Harper, Energy loss of 1–50 keV H, He, C, N, O, Ne, Ar ions transmitted through thin carbon foils. *Rev. Sci. Instrum.* **77**, 044501 (2006)
- F. Allegrini, R.W. Ebert, J. Alquiza, T. Broiles, C. Dunn, D.J. McComas, I. Silva, P. Valek, J. Westlake, A mass analysis technique using coincidence measurements from the IBEX-Hi detector. *Rev. Sci. Instrum.* **79**, 096107 (2008)
- F. Allegrini, G.B. Crew, D. Demkee, H.O. Funsten, D.J. McComas, B. Randol, B. Rodriguez, P. Valek, S. Weidner, The IBEX background monitor. *Space Sci. Rev.* (2009, this issue)
- D.A. Dahl, SIMION for the personal computer in reflection. *Int. J. Mass Spectrom.* **200**, 3 (2000)
- H.O. Funsten, D.J. McComas, B.L. Barraclough, Thickness uniformity and pinhole density analysis of thin carbon foils using keV ions. *Nucl. Instrum. Meth. B* **66**, 470 (1992)
- H.O. Funsten, D.J. McComas, B.L. Barraclough, Ultrathin foils used for low energy neutral atom imaging of planetary magnetospheres. *Opt. Eng.* **32**, 3090 (1993)
- H.O. Funsten, D.J. McComas, M.A. Gruntman, Energetic neutral atom imaging of the outer heliosphere–LIC interaction region, in *The Outer Heliosphere: The Next Frontiers*, ed. by K. Scherer, H. Fichtner, H.-J. Fahr, E. Marsch. COSPAR Colloquia Series, vol. 11 (Pergamon, New York, 2001), pp. 237–244
- H.O. Funsten, R.W. Harper, D.J. McComas, Absolute detection efficiency of space-based ion mass spectrometers and neutral atom imagers. *Rev. Sci. Instrum.* **76**, 053301 (2005)
- S.A. Fuselier, A.G. Ghielmetti, E. Hertzberg, A. Moore, D. Isaac, J. Hamilton, C. Tillier, E. Moebius, M. Granoff, D. Heitzler, B. King, H. Kucharek, S. Longworth, J. Nolin, S. Turco, P. Wurz, M. Wieser, J. Scheer, L. Saul, C. Schlemm, D.J. McComas, D. Chornay, J. Lobell, T. Moore, P. Rosmarynowski, R.J. Nemanich, T. Friedmann, H. Funsten, The IBEX-Lo sensor for the IBEX mission. *Space Sci. Rev.* (2009, this issue)
- G. Gloeckler, J. Geiss, Composition of the local interstellar medium as diagnosed with pickup ions. *Adv. Space Res.* **34**, 53 (2004)
- M.A. Gruntman, A.A. Kozochkina, V.B. Leonas, Multielectron secondary emission from thin foils bombarded by accelerated beams of atoms. *JETP Lett.* **51**, 22 (1990)
- M.A. Gruntman, Energetic neutral atom imaging of space plasmas. *Rev. Sci. Instrum.* **68**, 3617 (1997)
- M.A. Gruntman, E.C. Roelof, D.G. Mitchell, H.-J. Fahr, H.O. Funsten, D.J. McComas, Energetic neutral atom imaging of the heliospheric boundary region. *J. Geophys. Res.* **106**, 15767 (2001)
- M.G. Henderson, G.D. Reeves, H.E. Spence, R.B. Sheldon, A.M. Jorgensen, J.B. Blake, J.F. Fennell, First energetic neutral atom images from polar. *Geophys. Res. Lett.* **24**, 1167 (1997)
- D.C. Jones, J.D. Bernardin, Thermal modeling and experimental verification of the interstellar boundary explorer’s high energy neutral atom imaging instrument (IBEX-Hi), 2007 AIAA InfoTech at Aerospace Conference (2007), vol. 3, pp. 2364–2375
- R. Korde, C. Prince, D. Cunningham, R.E. Vest, E. Gullikson, Present status of radiometric quality silicon photodiodes. *Metrologia* **40**, S145 (2003)
- A.A. Kozochkina, V.B. Leonas, V.E. Fine, Statistics of heavy particle-induced electron emission from a foil, in *Ionization of Solids by Heavy Particles*, ed. by R.A. Baragiola (Plenum, New York, 1993), pp. 223–237

- D.J. McComas, F. Allegrini, C.J. Pollock, H.O. Funsten, S. Ritzau, G. Gloeckler, Ultra-thin (~ 10 nm) carbon foils in space instrumentation. *Rev. Sci. Instrum.* **75**, 4863 (2004)
- D.J. McComas, F. Allegrini, L. Bartolone, P. Bochsler, M. Bzowski, M. Collier, H. Fahr, H. Fichtner, P. Frisch, H. Funsten, S. Fuselier, G. Gloeckler, M. Gruntman, V. Izmodenov, P. Knappenberger, M. Lee, S. Livi, D. Mitchell, E. Möbius, T. Moore, S. Pope, D. Reisenfeld, E. Roelof, H. Runge, J. Scherrer, N. Schwadron, R. Tyler, M. Wieser, M. Witte, P. Wurzel, G. Zank, The Interstellar Boundary Explorer (IBEX): Update at the End of Phase B, AIP Conference Proceedings, vol. 858, *Physics of the Inner Heliosheath: Voyager Observations, Theory, and Future Prospects* (2006), pp. 241–250
- D.J. McComas, F. Allegrini, J. Balonado, B. Blake, P.C. Brandt, J. Burch, J. Clemmons, W. Crain, D. Delapp, R. DeMajistre, D. Everett, H. Fahr, L. Friesen, H. Funsten, J. Goldstein, M. Gruntman, R. Harbaugh, R. Harper, H. Henkel, C. Holmlund, G. Lay, D. Mabry, D. Mitchell, U. Nass, C. Pollock, S. Pope, M. Reno, S. Ritzau, E. Roelof, E. Scime, M. Sivjee, R. Skoug, T.S. Sotirelis, M. Thomsen, C. Urdiales, P. Valek, K. Viherkanto, S. Weidner, T. Ylikorpi, M. Young, J. Zoennchen, The Two Wide-angle Imaging Neutral-atom Spectrometers (TWINS) NASA mission-of-opportunity. *Space Sci. Rev.* **142**, 157 (2009a)
- D.J. McComas, F. Allegrini, P. Bochsler, M. Bzowski, M. Collier, H. Fahr, H. Fichtner, P. Frisch, H. Funsten, S. Fuselier, G. Gloeckler, M. Gruntman, V. Izmodenov, P. Knappenberger, M. Lee, S. Livi, D. Mitchell, E. Möbius, T. Moore, S. Pope, D. Reisenfeld, E. Roelof, J. Scherrer, N. Schwadron, R. Tyler, M. Wieser, M. Witte, P. Wurzel, G. Zank, IBEX—Interstellar boundary explorer. *Space Sci. Rev.* (2009b, this issue)
- D.G. Mitchell, S.E. Jaskulek, C.E. Schlemm, E.P. Keath, R.E. Thompson, B.E. Tossman, J.D. Boldt, J.R. Hayes, G.B. Andrews, N. Paschalidis, D.C. Hamilton, R.A. Lundgren, E.O. Tums, P. Wilson, H.D. Voss, D. Prentice, K.C. Hsieh, C.C. Curtis, F.R. Powell, High energy neutral atom (HENA) imager for the IMAGE mission. *Space Sci. Rev.* **91**, 67 (2000)
- H. Moestue, The electric field and geometrical factor of an annular curved plate electrostatic analyzer. *Rev. Sci. Instrum.* **44**, 1709 (1973)
- T.E. Moore, D.J. Chornay, M.R. Collier, F.A. Herrero, J. Johnson, M.A. Johnson, J.W. Keller, J.F. Laudadio, J.F. Lobell, K.W. Ogilvie, P. Rozmarynowski, S.A. Fuselier, A.G. Ghielmetti, E. Hertzberg, D.C. Hamilton, R. Lundgren, P. Wilson, P. Walpole, T.M. Stephen, B.L. Peko, B. Van Zyl, P. Wurzel, J.M. Quinn, G.R. Wilson, The low-energy neutral atom imager for IMAGE. *Space Sci. Rev.* **91**, 155 (2000)
- G. Paschmann, E.G. Shelley, C.R. Chappell, R.D. Sharp, L.F. Smith, *Rev. Sci. Instrum.* **41**, 1706 (1970)
- C.J. Pollock, K. Asamura, J. Balonado, M.M. Balkey, P. Barker, J. Burch, E.J. Korpela, J. Cravens, G. Dirks, M.-C. Fok, H.O. Funsten, M. Grande, M. Gruntman, J. Hanley, J.-M. Jahn, M. Jenkins, M. Lampton, M. Marckwordt, D.J. McComas, T. Mukai, G. Penegor, S. Pope, S. Ritzau, M.L. Schattenburg, E. Scime, R. Skoug, W. Spurgeon, T. Stecklein, S. Storms, C. Urdiales, P. Valek, J.T.M. van Beek, S.E. Weidner, M. Wüest, M.K. Young, C. Zinsmeyer, Medium Energy Neutral Atom (MENA) imager for the IMAGE mission. *Space Sci. Rev.* **91**, 113 (2000)
- F.H. Read, N.J. Bowring, P.D. Bullivant, R.R.A. Ward, Penetration of electrostatic fields and potentials through meshes, grids, or gauzes. *Rev. Sci. Instrum.* **69**, 2000 (1998)
- S.M. Ritzau, R.A. Baragiola, Electron emission from carbon foils induced by keV ions. *Phys. Rev. B* **58**, 2529 (1998)
- E.C. Roelof, D.G. Mitchell, D.J. Williams, Energetic neutral atoms ($E \approx 50$ keV) from the ring current: IMP 7/8 and ISEE 1. *J. Geophys. Res.* **90**, 991 (1985)
- E.G. Shelley, A.G. Ghielmetti, H. Balsiger, R.K. Black, J.A. Bowles, R.P. Bowman, O. Bratschi, J.L. Burch, C.W. Carlson, A.J. Coker, J.F. Drake, J. Fischer, J. Geiss, A. Johnstone, D.L. Kloza, O.W. Lennartson, A.L. Magoncelli, G. Paschmann, W.K. Peterson, H. Rosenbauer, T.C. Sanders, M. Steinacher, D.M. Walton, B.A. Whalen, D.T. Young, The toroidal imaging mass-angle spectrograph (TIMAS) for the Polar mission. *Space Sci. Rev.* **71**, 497 (1995)
- O.L. Vaisberg et al., Complex plasma analyzer SKA-1, in *Interball: Mission and Payload*, ed. by A.A. Galeev (Russian Space Agency–French Space Agency, 1995), pp. 170–177
- P. Wurzel, A. Galli, S. Barabash, A. Grigoriev, Energetic Neutral Atoms from the Heliosheath. *Astrophys. J.* **683**, 248 (2008)
- P. Wurzel, J. Scheer, L. Saul, S.A. Fuselier, A.G. Ghielmetti, E. Hertzberg, E. Möbius, H. Kucharek, H.O. Funsten, P. Janzen, R. Harper, M. Wieser, P.C. Brandt, E. Roelof, D. McComas, F. Allegrini, IBEX Backgrounds and signal to noise ratio. *Space Sci. Rev.* (2009, this issue)
- J.F. Ziegler, J.P. Biersack, U. Littmark, *Stopping and Range of Ions in Solids*, vol. 1 (Pergamon, New York, 1985)